

Using Persistent Homology Topological Features to Characterize Medical Images: Case Studies on Lung and Brain Cancers

Chul Moon^{*1}, Qiwei Li², and Guanghua Xiao³

¹Department of Statistical Science, Southern Methodist University, Dallas, TX, USA

²Department of Mathematical Sciences, University of Texas at Dallas, Richardson, TX, USA

³Quantitative Biomedical Research Center, Department of Population & Data Sciences and Department of Bioinformatics, University of Texas Southwestern Medical Center, Dallas, TX, USA

Abstract

Tumor shape is a key factor that affects tumor growth and metastasis. This paper proposes a topological feature computed by persistent homology to characterize tumor progression from digital pathology and radiology images and examines its effect on the time-to-event data. The proposed topological features are invariant to scale-preserving transformation and can summarize various tumor shape patterns. The topological features are represented in functional space and used as functional predictors in a functional Cox proportional hazards model. The proposed model enables interpretable inference about the association between topological shape features and survival risks. Two case studies are conducted using consecutive 143 lung cancer and 77 brain tumor patients. The results of both studies show that the topological features predict survival prognosis after adjusting clinical variables, and the predicted high-risk groups have significantly (at the level of 0.001) worse survival outcomes than the low-risk groups. Also, the topological shape features found to be positively associated with survival hazards are irregular and heterogeneous shape patterns, which are known to be related to tumor progression.

Keywords: *Topological Data Analysis, Tumor Shape, Functional Data Analysis, Survival Analysis, Cox Proportional Hazards Model*

^{*}Corresponding author. Email: chulm@smu.edu

1 Introduction

Recent advancements in the field of medical imaging lead to a high-resolution and informative description of human cancer. The Artificial Intelligence (AI) image processing algorithms, such as deep learning, have been developed to extract information from medical images and attained comparable achievements with human experts (Havaei et al., 2017; Levine et al., 2019; Wang et al., 2019). These AI algorithms also enable efficient medical image segmentation, which classifies image patches into categories such as tumors and normal regions. With such developments, medical images have a significant influence on medical decision making. Radiomics has been developed for decision support by extracting quantitative features of images and providing data for further analyses (Gillies et al., 2016; Rizzo et al., 2018). The two of the most common types of features of tumors are texture and shape (Bianconi et al., 2018). The textural features summarize the area, kurtosis, entropy, and correlation computed from pixel intensity and the gray-level co-occurrence matrix (Haralick et al., 1973). The shape features mainly focus on the boundaries of segmented tumor regions and quantify their roughness or irregularities (Bharath et al., 2018; Brú et al., 2008; Kilday et al., 1993; Bookstein, 1997; Zhang et al., 2020; Crawford et al., 2020). However, the existing features provide only a limited explanations about the tumor shape in that detailed local patterns such as a relationship, distribution, and connectivity between tumor and normal regions are not summarized. Also, the features developed to deal with radiographic images could be inadequate in high-resolution pathology images (Madabhushi and Lee, 2016; Zhang et al., 2020). In this paper, we propose using topological features computed by persistent homology to quantify various aspects of tumor shape features in the AI-segmented medical images.

Topological data analysis is a recently emerged area of study that investigates the shape of data using their topological features. Persistent homology is a commonly used topological data analysis tool that analyzes the shape of data with the multi-scale topological lens (Edelsbrunner and Harer, 2008; Carlsson, 2009). Persistent homology provides a numeric summary of the shape that is robust to noise and insensitive to metrics (Chazal et al., 2017). Persistent homology has been applied to various tumor image analyses, including colorectal tumor region segmentation (Qaiser et al., 2016), clustering of Gleason score of

prostate cancer histology (Lawson et al., 2019; Berry et al., 2020), and hepatic tumor classification (Oyama et al., 2019). Only a few studies have focused on survival prediction using topological features of medical images. Crawford et al. (2020) propose the smooth Euler characteristics to describe a shape of tumor boundaries and develop a functional survival model. Although their approach suggests that topological features predict the survival outcomes of brain tumor patients, it is sensitive to image transformation, only analyzes an outer boundary of tumor regions, difficult to infer which shape features are relevant to survival outcomes, and the proposed survival model cannot consider censored data. Also, Somasundaram et al. (2021) show that persistent homology summary features of Computed Tomography (CT) images predict lung cancer patients' survivals. However, the proposed persistent homology summary features are difficult to interpret.

We propose topological shape features for AI-segmented medical images computed by persistent homology. We first develop the distance transform that can reveal the tumor shape of AI-segmented medical images. Persistent homology is computed based on the proposed distance transform values. Unlike the most existing shape features that only focus on a few large segmented tumor regions, the proposed approach quantifies all tumor patterns, such as shape, size, distribution, and connectivity. The proposed topological shape features are invariant to the scale-preserving transformation, such as rotation and translation, and applicable to various types of medical images, including pathology and radiology images.

Statistical inference on different tumor shapes and patterns in medical images can be achieved by using the proposed persistent homology shape features. However, persistent homology results are algebraic objects, and this makes it difficult to use them as inputs of machine learning and statistical models. Although persistent homology outputs can be summarized as numeric values, they are given as a multiset of intervals, not a vector. As a result, several methods have been suggested to vectorize persistent homology results by representing them in different spaces such as Euclidean space (Adcock et al., 2016; Bendich et al., 2016; Adams et al., 2017), functional space (Chazal et al., 2014; Chen et al., 2015; Bubenik, 2015; Adams et al., 2017; Berry et al., 2020), and reproducing kernel Hilbert space (Reininghaus et al., 2015; Kusano et al., 2016). In this paper, persistent homology results

are represented in a functional space to maintain interpretability and assign flexible weights to topological features. The functional summary of persistent homology shape information is implemented in a functional survival model as a functional predictor.

We consider the Functional Cox Proportional Hazards (FCoxPH) model to characterize the association between functional topological shape features and survival outcomes. Since Chen et al. (2011) propose the FCoxPH model, various approaches have been developed (Gellar et al., 2015; Lee et al., 2015; Qu et al., 2016; Kong et al., 2018; Hao et al., 2020). In our study, the dimension of functional predictors is reduced by Functional Principal Component Analysis (FPCA), one of the key techniques in functional data analysis (Yao et al., 2005; Müller and Stadtmüller, 2005; Hörmann et al., 2015; Happ and Greven, 2018). We select a finite number of basis functions by FPCA and use them in the FCoxPH model. We extend the FCoxPH model of Kong et al. (2018) to include multiple functional predictors obtained by persistent homology. The proposed FCoxPH model implements both clinical variables and functional persistent homology shape features and enables interpretable inference about tumor shape.

We conduct case studies on lung cancer pathology images and brain tumor Magnetic Resonance Imaging (MRI) images, both image data were collected as part of clinical routine procedures. The results show that the proposed shape features calculated from routine medical images can be used to predict patient prognosis. The predicted high- and low-risk groups show significant differences in survival outcomes for both lung cancer pathology image dataset (p -value = 8×10^{-9} and hazard ratio = 6.837) and brain tumor MRI image applications (p -value = 3×10^{-4} and hazard ratio = 2.483). Also, the simulation studies show that the proposed method is robust to false shape information of medical images. We find that the irregular tumor shapes and heterogeneous patterns are positively related to risks of death, which coincide with the aggressive tumor patterns. The proposed method enables in-depth shape analysis on the survival prognosis using topological tumor shape features of medical images.

The rest of the paper is organized as follows. Section 2 introduces background for topological data analysis. Section 3 proposes the topological features of medical images and their functional representations and the FCoxPH model. Section 4 presents applications

to lung cancer pathology and brain tumor MRI image data. Section 5 concludes the paper and discusses future research topics.

2 Background: Homology and Persistent Homology

We first introduce a short theoretical background of topology to define topological shape features. Consider a shape is given as a topological space \mathcal{S} . Homology studies geometric patterns of \mathcal{S} by examining its k -dimensional holes. For example, zero-dimensional holes are connected components, one-dimensional holes are loops, and two-dimensional holes are voids. These k -dimensional holes are often called the topological features of the shape. Let $H_k(\mathcal{S})$ denotes the k -th homology group of \mathcal{S} . The Betti number β_k is the rank of $H_k(\mathcal{S})$ and it counts the number of k -dimensional holes in \mathcal{S} . Figure 1 presents three topological spaces and their Betti numbers. For example, the triangle in Figure 1b is one connected component with one hole ($\beta_0 = 1$ and $\beta_1 = 1$). Similarly, the Betti numbers of the circle in Figure 1b is $\beta_0 = 1$ and $\beta_1 = 1$. Therefore, the Betti numbers of Figure 1b is two dimension-zero features and two dimension-one features ($\beta_0 = 2$ and $\beta_1 = 2$).

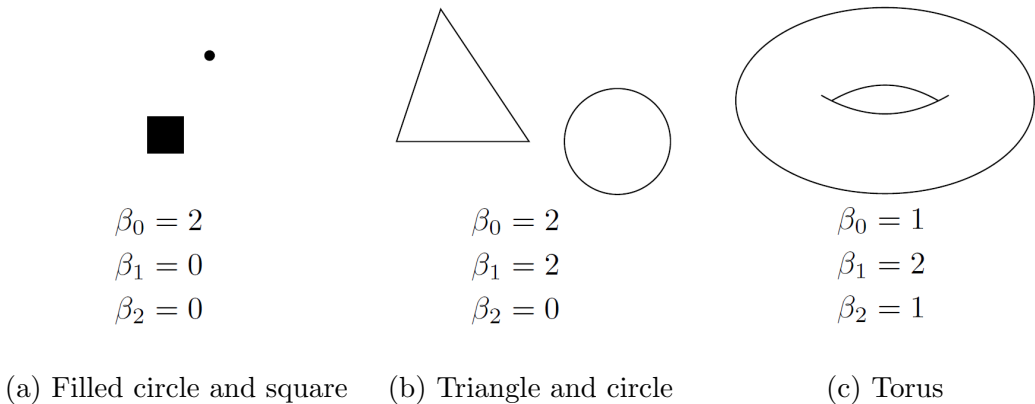


Figure 1: Topological space examples and their Betti numbers. β_0 , β_1 , and β_2 represent the number of zero-, one-, and two-dimensional holes.

Computing homology of topological space is challenging, albeit its simple concept. To overcome the computational issue, a topological space S is often approximated as a simplicial complex K . The simplicial complex is a finite set of simplices glued together. Examples of simplices are a point (0-simplex), line (1-simplex), triangle (2-simplex), and tetrahedron

(4-simplex). The discretized representation of shape enables computationally efficient homology computation (Edelsbrunner and Harer, 2008).

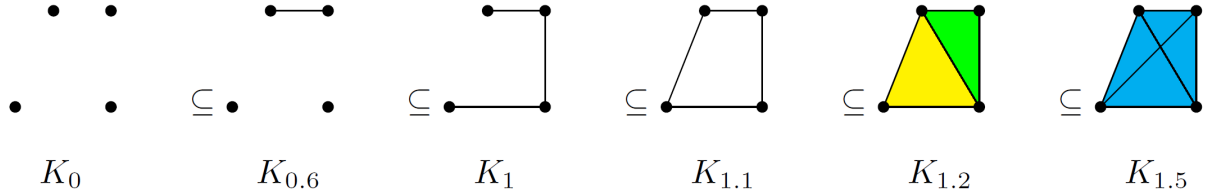
Persistent homology provides multi-scale homology representation of topological spaces. Let $\emptyset \subseteq K_{\epsilon_1} \subseteq K_{\epsilon_2} \subseteq \dots \subseteq K_{\epsilon_N}$ be a non-decreasing sequence of simplicial complices. Here, the inclusion \subseteq implies that a set of simplices on the left side of \subseteq is included on the right side of the simplicial complex. The index ϵ that controls the sequence is called the filtration. Figure 2a presents a sequence of simplicial complices, K_{ϵ} , with four vertices at $(0, 0)$, $(1, 0)$, $(1, 1)$, and $(0.4, 1)$. In K_{ϵ} , a $(k-1)$ -simplex is constructed if all pairwise distances between k vertices are less than or equal to ϵ . We see that homology evolves as the filtration value ϵ increases. For example, the 0-th Betti number of K_0 is $\beta_0 = 4$ as it has four disconnected points. On the other hand, $\beta_0 = 3$ in $K_{0.6}$ as the two points are connected.

The inclusion of K_{ϵ_i} in K_{ϵ_j} for $0 \leq \epsilon_i \leq \epsilon_j \leq \epsilon_N$ induces a map between the homology groups so that $0 \rightarrow H(K_{\epsilon_1}) \rightarrow H(K_{\epsilon_2}) \rightarrow \dots \rightarrow H(K_{\epsilon_N})$. The image of the map between homology groups includes information when a specific k -dimensional hole appears (birth) and disappears (death) over the filtration. Persistent homology computation result is given as multiple intervals of (birth, death). The length of the interval (death–birth) shows how long the topological feature persists.

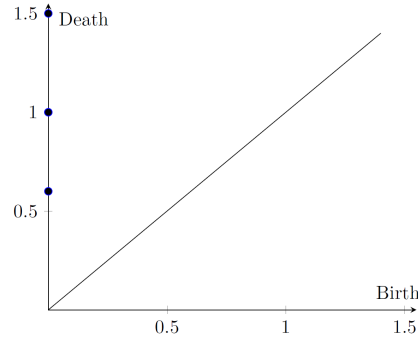
A persistence diagram is a collection of points in \mathbb{R}^2 where points in the diagram represent the birth and death values of features. Let $P = \{(b, d) \in \mathbb{R}^2 : b < d\}$ be a persistence diagram such that (b, d) denotes the birth and death values and \mathcal{D} be the space of persistence diagrams. The birth and death values can be plotted as points on the horizontal and vertical axis, respectively. Because the death of a topological feature comes after its birth, points of the persistence diagrams are placed above the diagonal line.

3 Topological Shape Analysis for Medical Images

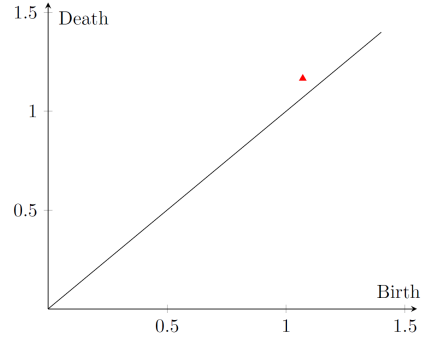
There are only a few studies that use topological features of medical images to predict patient survival outcomes. Recently, Crawford et al. (2020) use the Smooth Euler Characteristic Transform (SECT) to summarize the shape of the tumor boundary of glioblastoma multiforme (GBM) and predict the survival prognosis using Gaussian Process (GP) regression. Although their approach suggests that the summary of tumor shape paired with its



(a) Sequence of simplicial complices



(b) Dimension-zero persistence diagram



(c) Dimension-one persistence diagram

Figure 2: (a): Sequence of simplicial complices and its persistent homology results summarized as dimension-zero and dimension-one persistence diagrams. In K_ϵ , $k - 1$ -simplex if all pairwise distances between k vertices are less than or equal to ϵ . The dots and lines are vertices (0-simplices) and edges (1-simplices), respectively. The yellow- and green-colored regions in $K_{1.2}$ are triangles (2-simplices), and the blue-colored region in $K_{1.5}$ is a tetrahedron (3-simplices). (b)-(c): dimension-zero and dimension-one persistence diagrams of the simplicial complices (a).

location becomes useful, it comes with several limitations. First, the GP regression model cannot handle the right-censored datasets. Second, the SECT is sensitive to the rotation and orientation of images. This is challenging for some cases when medical images do not have a pre-defined direction. Third, it is difficult to interpret the GP regression result and provide clinical implications. To overcome the challenges, we propose using persistent homology to describe the shape of medical images.

3.1 Persistent Homology Shape Features of Medical Images

Persistent homology can reveal resourceful shape information when it is applied to image data. Especially, persistent homology applied to signed distance transformed binary material images successfully reveals pore structures and networks (Robins et al., 2016; Moon et al., 2019). However, the signed distance transform cannot be used to the three-class images because it is suitable for binary images.

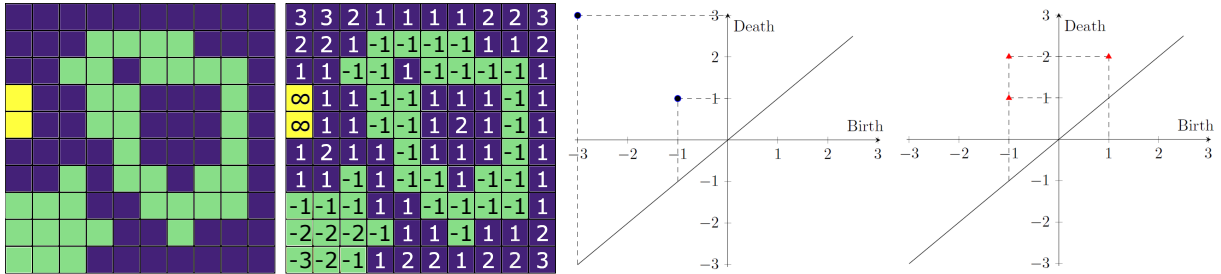
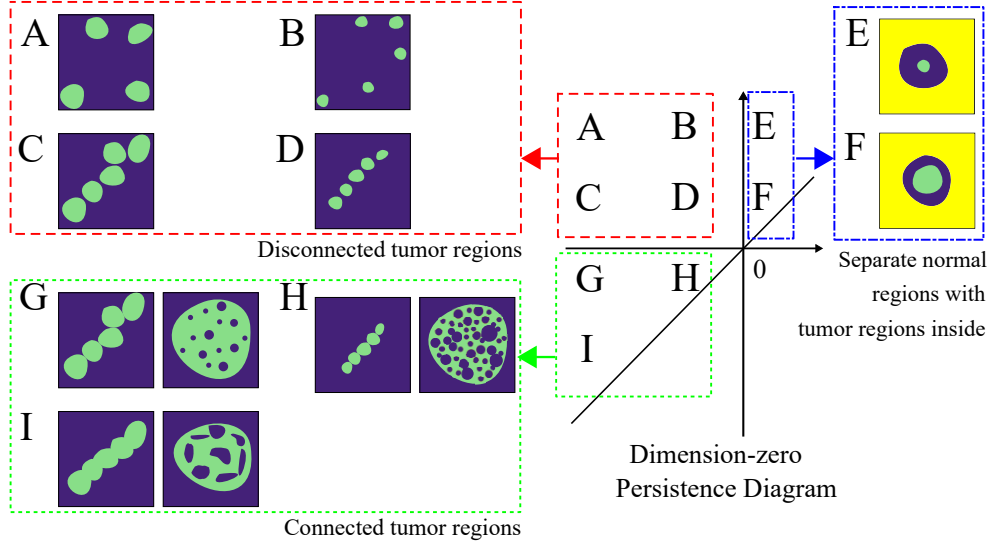


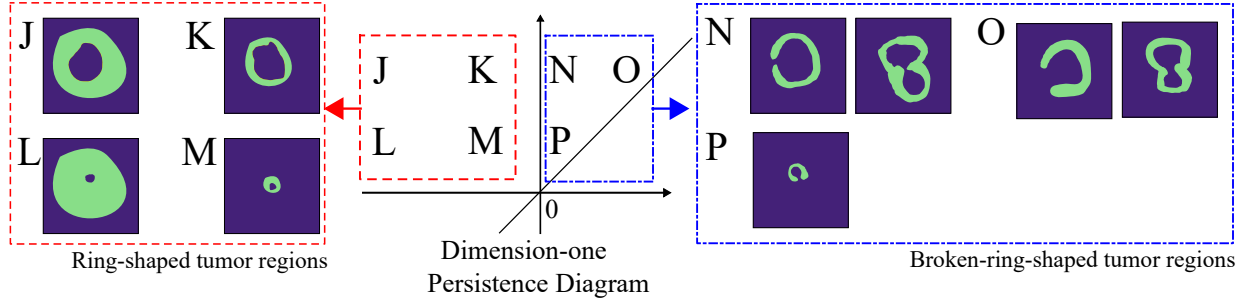
Figure 3: Three-class medical image example (left) and its signed distance assigned to each pixel using the taxicab distance (second from left), its dimension zero- and one-persistence diagrams (second from right and right, respectively). The green-, blue-, and yellow-colored pixels are tumor, normal, and empty regions, respectively.

We propose a Signed Euclidean Distance Transform for the three-class medical images (SEDT-3). Suppose that all pixels of medical images are classified into one of the three classes: tumor, normal, and empty regions. The three-class image itself does not reveal connectivity or size information. Structural and shape information can be discovered by using the distance transform. The proposed SEDT-3 assigns the shortest Euclidean distance to the other classes to each pixel. The sign of the SEDT-3 value depends on the classes; negative values for tumor region pixels, positive values for normal region pixels, and infinite values for the empty region pixels. The signed distance values have shape information in the sense that it shows connectivity and adjacency relationships between the neighboring pixels. Figure S1 presents the three-class medical image example and its signed distance transformed values. Here, a taxicab metric is used instead of a Euclidean distance for convenience.

We construct a cubical complex using the distance transform values to compute persistent homology. The cubical complex is a set of multi-dimensional cubes, such as points,



(a) Dimension-zero persistence diagram and the corresponding topological shape feature examples



(b) Dimension-one persistence diagram and corresponding topological shape feature examples

Figure 4: Interpretation of persistence diagrams of three-class medical images. The green, blue, and yellow colored pixels are tumor, normal, and empty regions, respectively.

lines, squares, and cubes, that are glued together. The cubical complex allows describing a structure of an image while preserving its topology (Couprie et al., 2001). We can obtain multi-scale shape information by computing persistent homology of the sequence of cubical complices. The empty regions are not used to construct cubical complices, so they do not directly affect persistent homology results. This is because the SEDT-3 assigns infinite value to empty region. See supplementary material for detailed illustrations of cubical complex construction and persistent homology computation.

Various tumor shapes can be summarized by the proposed persistent homology approach and they are recorded in different areas of persistence diagrams. Figure 4 illustrates

the areas of dimension-zero and dimension-one persistence diagrams and the examples of the shape features. See supplementary material for more detailed interpretation of the computed shape features.

The proposed persistent homology shape features are invariant to scale-preserving transformations, which include rotation, translation, and reflection. Our features only depend on the relative locations between the nearest other phase-regions. Therefore, the proposed approach is automatically invariant to rotations and orientation shifts.

We note that the size of features is measured by the radius of the largest circle that can be placed inside. Also, dimension-zero and dimension-one features are not exclusive; the pixels used to construct dimension-zero features can be used to build dimension-one feature and vice versa. For example, tumor regions in Figure 4b are also counted as dimension-zero features.

3.2 Functional Representation of Persistent Homology Shape Features

Although persistence diagrams include topological persistence signal information, it is not easy to use them directly as input in data analysis. This is because persistence diagrams are not in a common data type that most statistical models use. In our study, we represent persistence diagrams as persistence surface functions in a functional space inspired by Chen et al. (2015) and Adams et al. (2017).

The persistence surface function ρ_P of the persistence diagram P can be defined as

$$\rho_P(x, y) = \sum_{(b, d) \in P} g_{(b, d)}(x, y) \cdot w(b, d),$$

where x and y are the (x, y) -coordinates of the persistence surface function, $g_{(b, d)}$ is a smoothing function for $(b, d) \in P$, and $w(b, d) \geq 0$ is a non-negative weight function. A persistence surface function is a stable representation of a persistence diagram; persistence surface functions are robust to small perturbations of points in persistence diagrams (Adams et al., 2017). Figure 5 illustrates a persistence diagram and its functional representation.

When the proposed persistent homology approach is applied to the 2D medical images, two persistence surface functions will be obtained: dimension-zero and dimension-one.

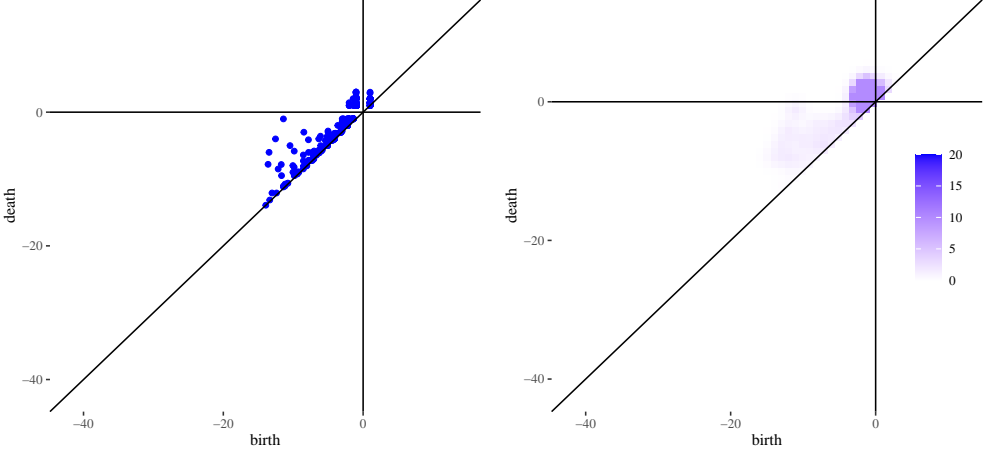


Figure 5: Persistence diagram (left) and persistence surface function (right).

We denote persistence surface functions of dimension-zero and dimension-one diagrams of subject i by X_i^0 and X_i^1 , respectively.

The weight function $w(b, d)$ allows assigning different importance to points in persistence diagrams. For example, long-persisting features could be more important than the short-living features in some applications. In this case, one can assign heavier weights to the points far from the diagonal. Various weights have been suggested, such as weights only depend on persistence of features (Chen et al., 2015; Adams et al., 2017; Kusano et al., 2016) and birth, death, and persistence values (Berry et al., 2020). In this paper, we use the maximum distance weight $w(b, d) = \max\{|b|, |d|, d - b\}$ that assigns heavier weights to features far from the origin of persistence diagrams.

We use the Gaussian smoothing function $g_{(b,d)}(x, y) = \frac{\exp[-((x-b)^2 + (y-d)^2)]}{\sigma^2}$ in the persistence surface function. The Gaussian smoothing function requires the selection of smoothing parameter σ . We denote the smoothing parameters for dimension-zero and dimension-one persistence surface functions as σ_0 and σ_1 . In our study, the smoothing parameters are determined by the Leave-One-Out Cross-Validation (LOOCV) using 900 combinations of σ_0 and σ_1 over the 2D grid expanded by $[0.1, 3]$ with a step size 0.1.

3.3 Cox Regression Model for Functional Data

A Cox Proportional Hazards (CoxPH) model (Cox, 1972) is a commonly used model to investigate the association between patients' survival prognosis and predictor variables. The hazard function with a p -dimensional scalar predictor $Z = (z_1, \dots, z_p)^T$ has the form

$$h(t) = h_0(t) \exp(Z^T \gamma), \quad (1)$$

where h_0 is the baseline hazard function and $t \in [0, \tau]$ for $0 < \tau < \infty$. We aim to conduct the FCoxPH model that uses a set of clinical predictor γ and two functional predictors X^0 and X^1 as

$$h(t) = h_0(t) \exp \left(Z^T \gamma + \int X^0(u) \alpha(u) du + \int X^1(v) \beta(v) dv \right). \quad (2)$$

The objective of the FCoxPH model is to determine the unknown coefficients γ , α , and β . Due to the infinite dimensionality of functional data, dimension reduction is often required. We use FPCA to represent functional data in a lower-dimensional space. Let X_i^0 and X_i^1 be the persistence surface functions of medical image i and $\mu^0(u) = E[X_i^0(u)]$ and $\mu^1(v) = E[X_i^1(v)]$ be the mean functions of X_i^0 and X_i^1 . By the spectral decomposition, the covariance functions can be represented as $\text{Cov}(X_i^0(u), X_i^0(u')) = \sum_{j=1}^{\infty} \lambda_j \phi_j(u) \phi_j(u')$ and $\text{Cov}(X_i^1(v), X_i^1(v')) = \sum_{k=1}^{\infty} \delta_k \pi_k(v) \pi_k(v')$, where $\{\lambda_j\}_{j \geq 1}$ and $\{\delta_k\}_{k \geq 1}$ are non-increasing eigenvalues and $\{\phi_j\}_{j \geq 1}$ and $\{\pi_k\}_{k \geq 1}$ are orthonormal eigenfunctions of $X_i^0(u)$ and $X_i^1(v)$. By the Karhunen-Loève expansion (Karhunen, 1947; Loève, 1946), the persistence surface functions X_i^0 and X_i^1 can be expressed as

$$X_i^0(u) = \mu^0(u) + \sum_{j=1}^{\infty} \xi_{ij} \phi_j(u), \quad X_i^1(v) = \mu^1(v) + \sum_{k=1}^{\infty} \zeta_{ik} \pi_k(v),$$

where $\xi_{ij} = \int (X_i^0(u) - \mu^0(u)) \phi_j(u) du$ and $\zeta_{ik} = \int (X_i^1(v) - \mu^1(v)) \pi_k(v) du$ are the Functional Principal Component (FPC) scores of dimension-zero and dimension-one, respectively. The FPC scores have mean zero $E[\xi_{ij}] = E[\zeta_{ik}] = 0$ with covariances $E[\xi_{ij} \xi_{ij'}] = \lambda_j 1(j = j')$ and $E[\zeta_{ik} \zeta_{ik'}] = \delta_k 1(k = k')$ where $1(\cdot)$ is an indicator function. We can approximate functional data $X_i^0 \approx \mu^0(u) + \sum_{j=1}^q \xi_{ij} \phi_j(u)$ and $X_i^1 \approx \mu^1(v) + \sum_{k=1}^r \zeta_{ik} \pi_k(v)$, where q and r are the selected number of eigenfunctions. Then the FCoxPH model (2) can be

approximated as

$$h_i(t) \approx h_0^*(t) \exp \left(Z_i^T \gamma + \sum_{j=1}^q \xi_{ij} \alpha_j + \sum_{k=1}^r \zeta_{ik} \beta_k \right), \quad (3)$$

where $h_0^*(t) = h_0(t) \exp \left(\int \mu^0(u) \alpha(u) du + \int \mu^1(v) \beta(v) dv \right)$. The dimension of predictors is reduced to $p + q + r$ in the FCoxPH model (3). We can obtain the estimated coefficients using the selected eigenfunctions and their estimated coefficients as $\hat{\alpha}(u) \approx \sum_{j=1}^q \hat{\alpha}_j \hat{\phi}_j(u)$ and $\hat{\beta}(v) \approx \sum_{k=1}^r \hat{\beta}_k \hat{\pi}_k(v)$.

The FCoxPH model that incorporates the functional tumor shape predictors enables interpretable inference about the association between shape patterns and survival outcomes. The estimated functional coefficients $\hat{\alpha}(u)$ and $\hat{\beta}(v)$ inform which parts of persistence surface functions are associated with survival risks. The findings also can be presented by figures that plot the estimated coefficients on the space of a persistence surface function. By comparing the estimated coefficients plots and the shape features in Figure 4, one can see which shape patterns contribute the most to the hazard prediction.

Two criteria are used to select the number of FPCs for the FCoxPH models. First, the percentage of variance explained by the FPCs is used to determine q and r for validation tests. Let $PV^0(q) = \sum_{j=1}^q \lambda_j / \sum_{j=1}^{\infty} \lambda_j$ and $PV^1(r) = \sum_{k=1}^r \delta_k / \sum_{k=1}^{\infty} \delta_k$ be the percentages of variances explained by q dimension-zero and r dimension-one FPCs, respectively. For a given variability threshold C , the minimum number of FPCs that exceed the threshold: $q = \min\{q : PV^0(q) > C\}$ and $r = \min\{r : PV^1(r) > C\}$. Second, the Akaike information criterion (AIC) is used to choose the number of the FPCs for estimating the FCoxPH models (Yao et al., 2005). Let $L(\gamma_1, \dots, \gamma_p, \alpha_1, \dots, \alpha_q, \beta_1, \dots, \beta_r \mid q, r)$ denote the partial likelihood function of the FCoxPH model (3) given the number of the FPCs q and r . The AIC value of the FCoxPH model is $AIC(q, r) = 2(q+r) - 2 \log\{L(\hat{\gamma}_1, \dots, \hat{\gamma}_p, \hat{\alpha}_1, \dots, \hat{\alpha}_q, \hat{\beta}_1, \dots, \hat{\beta}_r \mid q, r)\}$. We determine an optimal number of components q and r by computing the AIC under the various combinations of q and r . For the tied event times, we use the approximation method of Efron (1977) to adjust the partial likelihood. Kong et al. (2018) show by simulation studies that the percentage of variance criterion and the AIC criterion are suitable for validation tests and model estimation for the FCoxPH model, respectively.

4 Case Studies

4.1 Application to Lung Cancer Pathology Images

Lung cancer is one of the most deadly cancers (Siegel et al., 2020). One of the most common types of lung cancer is adenocarcinoma that accounts for about 40% of all lung cancers (Zappa and Mousa, 2016), and it has various morphological features (Matsuda and Machii, 2015). We use 246 pathology images of 143 lung adenocarcinoma patients in the National Lung Screening Trial (NLST) data. All images are obtained under 40X magnification, and the median size of images is $24,244 \times 19,261$ pixels. The image patches of size 300×300 pixels (75×75 microns) are segmented into three classes of tumor, normal, and empty regions using a deep convolutional neural network (Wang et al., 2018). We implement an additional pre-processing step to remove noise: a single pixel is considered to be noise when its class is different from the surrounding eight singular-class pixels and the noise pixels are reclassified to the class of the surrounding pixels. The denoised three-class images are transformed using the SEDT-3. Figure 6 presents the pathology image, segmented three-class image of Wang et al. (2018) and the SEDT-3 transformed image.

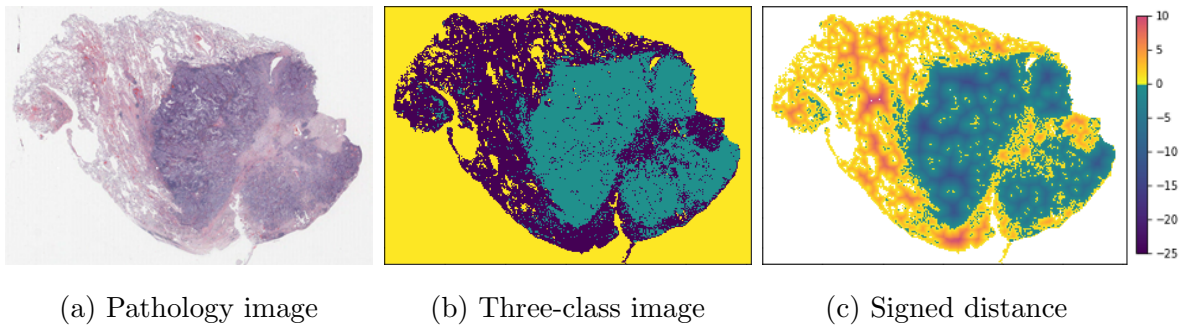


Figure 6: The lung adenocarcinoma pathology image (left), three-class pathology image segmented by Wang et al. (2018) (middle), and signed Euclidean distance transformed image (right). In the three-class image, the green, purple, and yellow colored pixels are tumor, normal, and empty regions. In the signed distance transformed image, tumor regions are colored from blue to green and normal regions are colored yellow to red.

A sequence of cubical complices is constructed using the SEDT-3 values as filtration, and persistent homology is computed using GUDHI (Dlotko, 2015). We exclude the intervals

with infinite death values to remove features related to empty regions. The median number of the computed features per image slice is 694 for dimension-zero and 1,768 for dimension-one. The ranges of persistence diagrams are (-41, 11) for dimension-zero and (-19, 26) for dimension-one.

The computed persistence diagrams are represented as the persistence surface functions using the Gaussian smoothing kernel with the maximum distance weight. Multiple smoothing parameter combinations are selected by the LOOCV and we use the smoothing parameters $\sigma_0 = 2$ and $\sigma_1 = 0.9$. See supplementary material for the complete list of the selected smoothing parameter combinations. We observe the persistence surface functions on grid points at the center of the square lattices of size one, on and above the diagonal line.

4.1.1 Model Estimation

We construct the CoxPH model using the following scalar clinical predictors: age, sex, smoking status, stage of cancer (I to IV), and tumor size. The size of tumor is measured by the number of tumor pixels in an image slice. Also, we fit the FCoxPH model using the functional predictors and the same clinical predictors used in the CoxPH model. The AIC criterion yield three selected FPCs: one FPC for dimension-zero ($q = 1$) and two FPCs for dimension-one ($r = 2$). For both models, we assume the baseline hazard function $h_0(t) = 1$.

Table 1 shows the results of the CoxPH and FCoxPH models. Among the clinical predictors in both models, age and stage III and IV indicators have the p-values smaller than 0.05. In the FCoxPH model, the p-values of all selected FPCs are smaller than 0.05. The overall p-values of the Wald tests are 2×10^{-4} for the CoxPH model and 1×10^{-6} for the FCoxPH model. The clinical variables behave similarly for both models except for the tumor size predictor. The p-value of the tumor size variable increases in the FCoxPH model as the functional predictors are added, suggesting that one of the functional predictors may include the tumor size information.

The estimated coefficients of persistence surface functions, $\hat{\alpha}(u)$ and $\hat{\beta}(v)$, show which shape features affect the survival prognosis and how they are related. Figure 7 shows the estimated functional coefficients. The blue-colored and red-colored areas have positive and

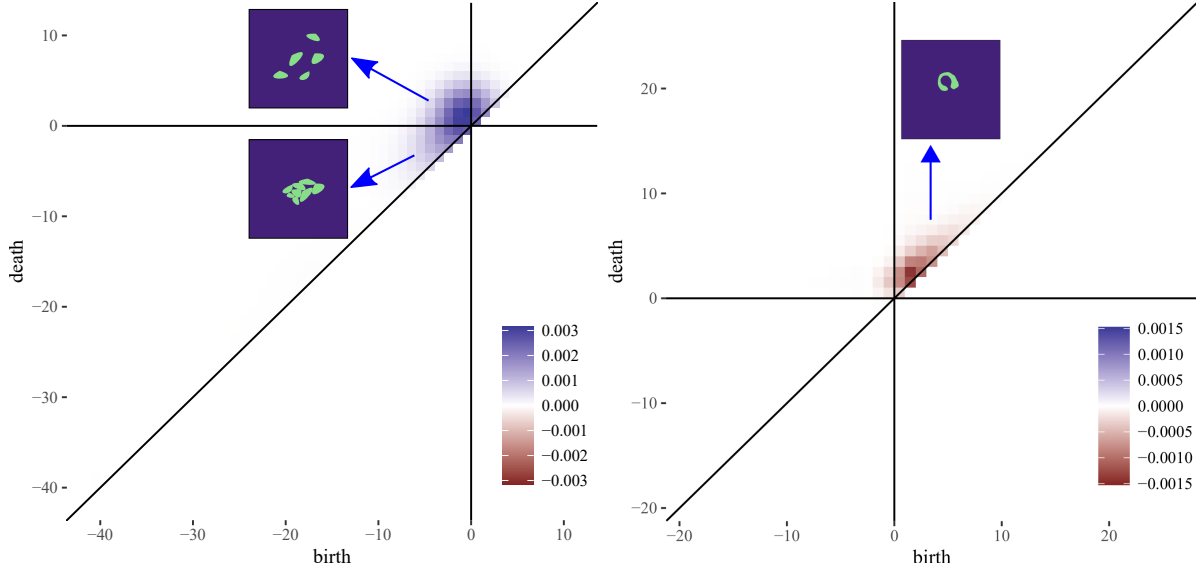
Table 1: The outputs of the Cox proportional hazards (CoxPH) and functional Cox proportional hazards (FCoxPH) models of the lung cancer adenocarcinoma patients. The ‘coef.’ and ‘SE’ are abbreviations of the coefficient and standard error, respectively. The p-values smaller than 0.05 are marked in bold.

	CoxPH model				FCoxPH model			
	coef.	$e^{\text{coef.}}$	SE	p-value	coef.	$e^{\text{coef.}}$	SE	p-value
Age	0.084	1.088	0.023	0.007	0.083	1.087	0.024	0.013
Smoker vs. non-smoker	-0.067	0.935	0.262	0.831	-0.253	0.776	0.234	0.426
Female vs. male	0.081	1.085	0.235	0.803	0.088	1.092	0.242	0.791
Tumor size	<0.001	1.000	<0.001	0.084	<0.001	1.000	<0.001	0.572
Stage II vs. stage I	0.545	1.725	0.382	0.366	0.477	1.611	0.390	0.432
Stage III vs. stage I	1.195	3.304	0.270	0.002	1.170	3.222	0.277	0.002
Stage IV vs. stage I	1.442	4.227	0.342	0.002	1.424	4.152	0.346	0.003
Dimension 0, 1 st FPC	-	-	-	-	0.013	1.001	0.003	<0.001
Dimension 1, 1 st FPC	-	-	-	-	-0.002	0.998	<0.001	0.002
Dimension 1, 2 nd FPC	-	-	-	-	0.002	1.002	<0.001	0.001

negative effects on the hazard function, respectively.

The topological features recorded in the blue-colored areas on the quadrant II and III of Figure 7a correspond to the aggressive tumor patterns. First, the colored area in quadrant II in Figure 7a represents the small-sized scattered tumor regions close to each other (i.e., see the example of area D in Figure 4a). Also, quadrant III of Figure 7a represents the relatively small connected tumor shapes. The small connected tumor features are spotted where multiple tumor regions spread inside normal (i.e., see the examples of area H in Figure 4a). These patterns imply a fast spread of tumors.

On the other hand, the shapes appear in the red-colored regions in quadrant I of Figure 7b match with less aggressive tumor behaviors. The red-colored region corresponds to broken-ring shaped tumor regions (i.e., see the examples of areas N, P, and O in Figure 4b). These shapes require an ample-sized normal region that could be surrounded by tumor but not invaded by tumor. If a small tumor region penetrates the normal region in-



(a) Dimension-zero functional coefficient $\hat{\alpha}(u)$ (b) Dimension-one functional coefficient $\hat{\beta}(v)$

Figure 7: Estimated coefficient functions $\hat{\alpha}(u)$ and $\hat{\beta}(v)$ of the functional Cox proportional hazards model of the lung adenocarcinoma patients. The estimated coefficient functions are plotted on the spaces of the dimension-zero and dimension-one persistence diagrams. The tumor shape patterns that correspond to the non-zero coefficient regions are drawn.

side the broken-ring shaped tumor regions, the dimension-one features are not constructed. Therefore, the broken-ring shaped tumor may not likely to appear where the small tumor regions are densely populated. These results coincide with the findings that tumor shape complexity and heterogeneous spread are associated with prognosis (Yokoyama et al., 1991; Miller et al., 2003; Chatzistamou et al., 2010; Vogl et al., 2013; Grove et al., 2015) and tissue transport properties (Soltani and Chen, 2012; Sefidgar et al., 2014).

Another interesting observation is that the relatively small-sized topological features, approximately radius of up to 10 pixels (750 microns), have large effects on the hazard function. We see that the estimated non-zero functional coefficients, the colored regions in Figure 7, are close to the origin compared to the ranges of persistence surface functions. The topological features near the origin correspond to small-sized features that have small birth and death values. This indicates that valuable information about the lung cancer patients obtained by the proposed persistent homology approach is mainly about local shapes and patterns.

4.1.2 Validity Test

We examine the validity of topological features in the FCoxPH model for predicting the survival outcome. We conduct the chi-square test with $q + r$ degrees of freedom that uses the $q + r$ number of coefficients of functional basis,

$$H_0 : \alpha_1 = \alpha_2 = \dots = \alpha_q = \beta_1 = \dots = \beta_r = 0$$

$$H_1 : \alpha_j \neq 0 \text{ or } \beta_k \neq 0 \text{ for at least one } j \in \{1, 2, \dots, q\} \text{ or } k \in \{1, 2, \dots, r\}.$$

We use the percentage of variance explained by FPCs to select q and r . The variance threshold of $C = 90\%$ is used and two dimension-zero and two dimension-one functional basis are selected ($q = r = 2$). As a result, the chi-square test of degrees of freedom four is conducted. The computed p-value is 0.005, suggesting that the topological features are a strong signal. Therefore, aside from the clinical variables included in the model, the topological features offer additional information in predicting lung cancer patients' survival outcomes.

4.1.3 Prediction using Cross-validation

We predict the risk scores using the LOOCV for two models, the CoxPH model (1) and the FCoxPH model (3). For a given pathology image $I \in \{1, 2, \dots, 246\}$, the models are trained for the rest 245 images. The risk score of I is predicted using the trained model. We repeat it for all 246 images, and the predicted risk scores are averaged for each patient. We assign 143 patients into two groups of 71 high-risk patients and 72 low-risk patients using the median patient-wise risk score.

The proposed FCoxPH model shows a better separation between the two groups over the CoxPH model. The Kaplan-Meier plots of the high- and low-risk groups predicted by the two models are presented in Figure 8. The p-value of the log-rank test of the FCoxPH model is 8×10^{-9} , which is smaller than that of the CoxPH model 1×10^{-5} . The hazard ratios between the predicted high-risk group and the low-risk group of the FCoxPH and CoxPH models are 6.837 and 4.032, respectively.

Note that the GP model using SECT of Crawford et al. (2020) is not applied to the lung pathology image analysis in our study. First, the SECT is sensitive to the rotation

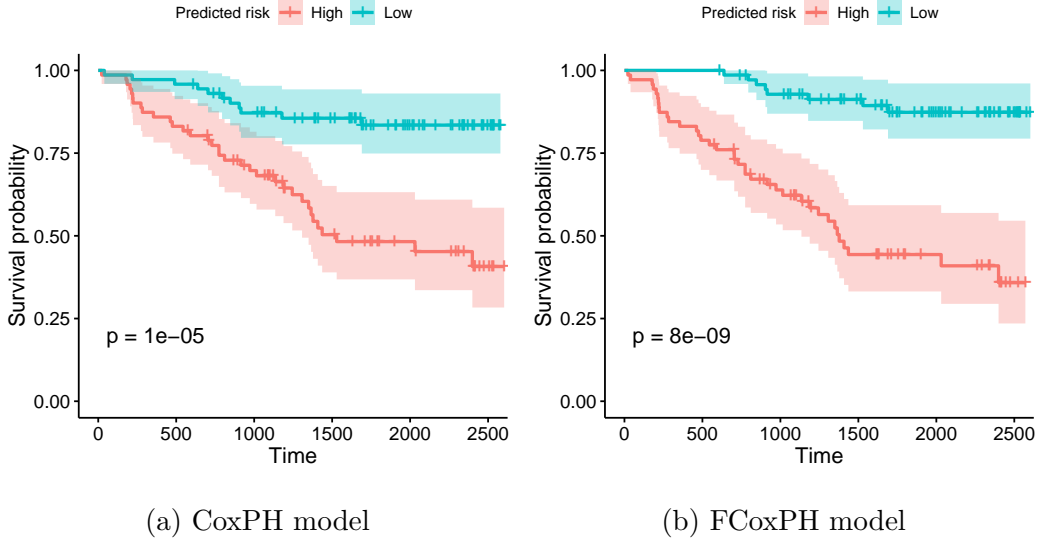


Figure 8: The Kaplan–Meier plots for the high- and low-risk groups of the Cox proportional hazards (CoxPH) and functional Cox proportional hazards (FCoxPH) models of the lung adenocarcinoma patients.

and location, making it unsuitable for pathology images. Also, about 69% of observations are right-censored (98 out of 143 patients), so the outcome of the GP model, which cannot consider censoring, is not reliable.

4.1.4 Prediction under False Shape Information

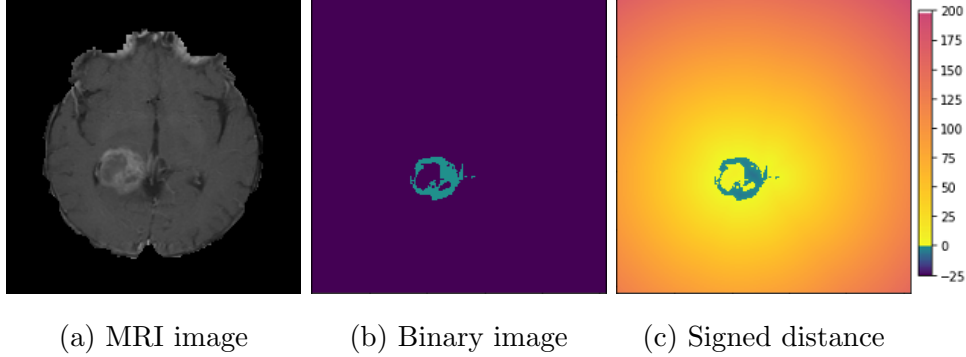
A simulation study is conducted to examine whether our method detects false positives. We make new images by randomly arranging the pixels from the existing three-class images to generate false shape information. The rearranged image retains the same proportions of the tumor, normal, and empty regions as the original image but loses shape information. We generate a total of 50 cohorts, each with 246 rearranged images. Persistent homology is computed, and computation outputs are represented as a persistence surface function using the same setting. For each cohort, we predict the risk scores using the LOOCV, assign high- and low-risk groups, and compute the p-values of the log-rank tests. If the FcoxPH model detects the false shape information, its functional shape predictors will have limited effect; thus, its p-value will be similar to that of the CoxPH model that only uses clinical variables.

The simulation result implies that the proposed FCoxPH model with false shape information has similar predictive power to the CoxPH model. Most p-values of the FCoxPH models with the rearranged images are similar to the p-value of the CoxPH model; only three p-values differ more than 1×10^{-4} compared to the p-value of the CoxPH model. This suggests that the false shape information has a limited impact in improving the prediction accuracy of the FCoxPH model. The distribution of the p-values of the FCoxPH models using the rearranged images is given in supplementary material.

4.2 Application to Brain Tumor MRI Images

GBM is the most common malignant grade IV brain tumor (Surawicz et al., 1999). GBM is distinguished from the lower-grade astrocytomas (grade II and III) by its accelerated growth rate. The rapid outward growth of GBM develops necrosis, and it is considered a hallmark of GBM. On T1-weighted contrast-enhanced imaging MRI, most GBM cases show a ring-shaped enhancement made of hypervascular tissues with a necrotic region at the center (Zhu et al., 2000; Henson et al., 2005). Figure 9a shows the MRI image of the GBM patient that has a ring-enhancing mass. The presence of necrosis is a significant prognosis factor (Nelson et al., 1983), and clinical studies show that the degree of necrosis is negatively associated with a survival rate (Hammoud et al., 1996; Raza et al., 2002). However, due to its irregular shape, multifocal enhancement, and the existence of multiple small lesions, evaluation of GBM shapes using MRI images could be difficult (Eisenhauer et al., 2009; Upadhyay and Waldman, 2011).

We use 77 GBM patients' MRI scans obtained from The Cancer Imaging Archive (TCIA) (Clark et al., 2013; Scarpace et al., 2016) and their clinical data retrieved from The Cancer Genome Atlas (TCGA) (Network et al., 2008). The MRI images are segmented into two classes of the tumor and non-tumor regions using the Medical Imaging Interaction Toolkit with augmented tools for segmentation (Chen and Rabadán, 2017). Each patient has approximately 23 to 25 segmented MRI images and the spaces between the MRI images are not the same. The size of images are either 256×256 or 512×512 . We only use 1,190 MRI images that have more than 100 tumor pixels because some images do not include tumor regions that are not large enough. The segmented binary images are



(a) MRI image (b) Binary image (c) Signed distance

Figure 9: The T1-weighted contrast-enhanced MRI image of GBM patient (left), segmented binary image (middle), and signed distance transformed image (right). In the binary image, the green and purple pixels are the tumor and non-tumor regions, respectively. In the signed distance transformed image, the tumor regions are colored from blue to green and the normal regions are colored yellow to red.

transformed by the SEDT for two-class (SEDT-2). The SEDT-2 is a simpler version of the SEDT-3; it does not assign infinite values because the binary images do not have empty regions. Figures 9b and 9c show the segmented binary image and distance transformed by the SEDT-2.

The topological shape features in the MRI images are obtained by computing persistent homology of cubical complex based on the SEDT-2 values. Interpretation of the topological shape features of the binary images are similar to those of the three-class images illustrated in Figure 4; there are no topological features that summarize the separate non-tumor regions (e.g., E and F in Figure 4a). Especially, the ring-shaped enhancements of the GBM patients' MRI images are recorded as dimension-one topological shape features. As illustrated in Figure 4b, the broken-ring- and unbroken-ring-shaped masses appear in quadrant I and II of the dimension-one persistence diagram, respectively.

The number of topological shape features of the GBM images is much smaller than that of the lung cancer pathology images. The median of the number of computed persistent homology features per image slice is 16 for dimension-zero and 17 for dimension-one, respectively. This is because MRI images are scanned in lower resolution than pathology images, and GBM tumors are smaller and simpler than lung cancer regions. Also, the persistent homology features obtained from the images of size 512×512 are divided by two

for a consistent comparison with the images of size 256×256 . The ranges of persistent homology shape summaries are $(-22, 26)$ for dimension-zero and $(-6, 32)$ for dimension-one. We represent the topological shape features as persistence surface functions using the smoothing parameters $\sigma_0 = 0.3$ and $\sigma_1 = 0.5$. See supplementary material for all smoothing parameters selected by the LOOCV. The mean persistence surface function is used to represent each patient’s tumor shape information.

4.2.1 Model Estimation

We fit the CoxPH and FCoxPH models to predict overall survival of the GBM patients. For both models, four clinical predictors are used: age, gender, Karnofsky performance score (KPS), and tumor size. The size of tumor is calculated by the average number of tumor pixels in each patient’s images. In the FCoxPH model, four FPCs (one dimension-zero ($q = 1$) and three dimension-one FPCs ($r = 3$)) are selected by AIC.

Table 2: The outputs of the Cox proportional hazards (CoxPH) and functional Cox proportional hazards (FCoxPH) models of glioblastoma multiforme patients. The ‘KPS’, ‘coef.’, and ‘SE’ are abbreviations of the Karnofsky performance score, coefficient, and standard error, respectively. The p-values smaller than 0.05 are marked in bold.

	CoxPH model				FCoxPH model			
	coef.	$e^{\text{coef.}}$	SE	p-value	coef.	$e^{\text{coef.}}$	SE	p-value
Age	0.028	1.028	0.012	0.022	0.034	1.035	0.013	0.009
Female vs. male	-0.084	0.920	0.321	0.794	-0.243	0.784	0.333	0.465
KPS	-0.015	0.985	0.010	0.125	-0.009	0.992	0.012	0.460
Tumor size	<0.001	1.000	<0.001	0.015	<0.001	1.000	<0.001	0.343
Dimension 0, 1 st FPC	-	-	-	-	-0.042	0.959	0.038	0.212
Dimension 1, 1 st FPC	-	-	-	-	0.077	1.081	0.032	0.016
Dimension 1, 2 nd FPC	-	-	-	-	0.008	1.008	0.028	0.769
Dimension 1, 3 rd FPC	-	-	-	-	0.100	1.105	0.038	0.008

Table 2 summarizes the results of the CoxPH and FCoxPH models. Age has the p-value smaller than 0.05 in both models and the size of tumor has p-value smaller than 0.05 in the

CoxPH model. In the FCoxPH model, the p-value of the two FPC scores are smaller than 0.05. The overall p-values of the Wald tests are 0.001 for the CoxPH model and 5×10^{-4} for the FCoxPH model.

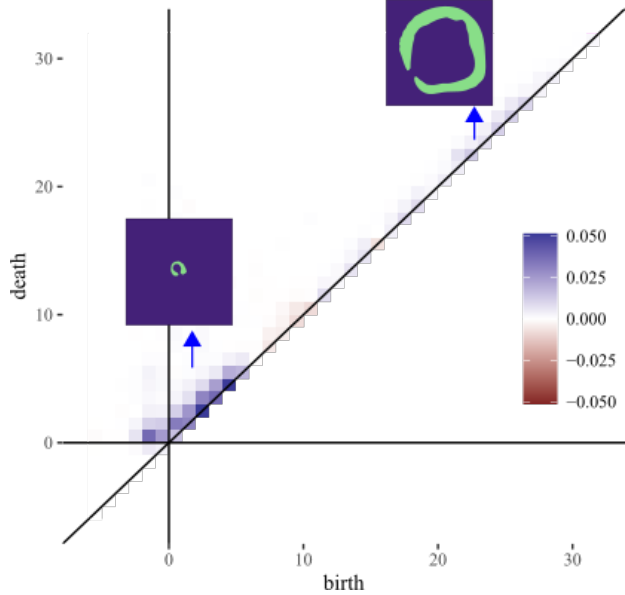


Figure 10: Estimated dimension-one coefficient function $\hat{\beta}(v)$ of the functional Cox proportional hazards model of the GBM patients. The estimated coefficient function is plotted on the space of the dimension-one persistence diagram.

Figure 10 presents the estimated coefficient of dimension-one persistence surface function $\hat{\beta}$ of the GBM patients. The blue-colored areas indicate that a larger number of small- and large-sized broken-ring-shaped features are associated with higher risks. These patterns are most likely to correspond to the large necrotic center and heterogeneous enhancement outside of the rim. The estimated coefficient of dimension-zero persistence surface function $\hat{\alpha}$ is not presented because it is not significant.

4.2.2 Validity Test

We conduct the chi-square test to examine validity of functional topological shape features obtained from the brain tumor MRI images. We use the variability threshold $C = 90\%$ and 11 dimension-zero FPCs ($q = 11$) and nine dimension-one FPCs ($r = 9$) are selected. The chi-square test statistic with degrees of freedom of 20 is 146.50 and its p-value is

close to zero. This implies that the proposed topological shape features are informative for predicting the survival outcomes of the GBM patients after adjusting the clinical variables.

4.2.3 Prediction using Cross-validation

We compare the prediction results of three models: CoxPH, FCoxPH, and the GP model of Crawford et al. (2020). For the CoxPH and FCoxPH models, we obtain the predicted risk scores by using the LOOCV and designate high- and low-risk groups of 38 and 39 patients, respectively. Unlike the CoxPH and FCoxPH models, the GP model predicts the standardized survival times of patients, and does not provide risk information. Therefore, we compute the predicted standardized survival times for the GP model by the LOOCV and assign 38 and 39 patients to the shorter- and longer-surviving groups, respectively. Since the GP model does not consider clinical predictors, only the topological shape summary obtained by the SECT is used as a predictor. Also, we use the Gaussian kernel in the GP model because it performs the best to predict overall survival (Crawford et al., 2020). We note that the six right-censored observations are used as a death time in the GP model because the model cannot handle the right-censored observations.

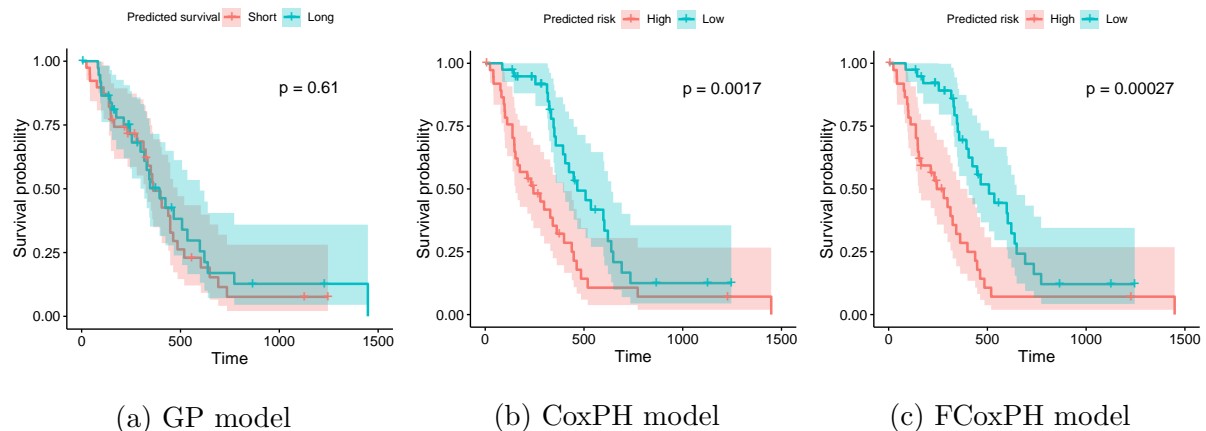


Figure 11: The Kaplan–Meier plots for the shorter- and longer-surviving groups of the Gaussian process (GP) model and the high- and low-risk groups of Cox proportional hazards (CoxPH), and functional Cox proportional hazards (FCoxPH) models of the GBM patients.

Figure 11 shows the Kaplan-Meier plots of the shorter- and longer-predicted surviving groups of the GP model and the high- and low-risk groups of the CoxPH and FCoxPH

models. The p-values of the log-rank tests are 0.61 for the GP regression model, 0.002 for the CoxPH model, and 3×10^{-4} for the FCoxPH model. The log-rank tests imply that the proposed persistent homology shape features captured provide a strong signal in predicting overall survival prognosis of the GBM patients after taking into account the clinical predictors. The hazard ratio between the predicted high-risk and low-risk groups is 2.233 for the CoxPH model and 2.483 for the FCoxPH model.

4.2.4 Prediction under False Shape Information

We also conduct a simulation study to test the false positives. We use the same simulation setting in Section 4.1.4: generate 50 cohorts with 77 GBM patients' pixel-rearranged MRI images, compute persistent homology shape features, and predict risk scores using the FCoxPH model by the LOOCV.

The simulation results suggest that the FCoxPH model detects false shape information. Most p-values of the FCoxPH models with the rearranged images are similar to that of the CoxPH model; only three p-values differ by more than 0.05. The p-values of the FCoxPH model with rearranged MRI images are summarized in supplementary material.

5 Conclusion

In this article, we propose a new summary statistic to represent the shape of tumors of medical images using their topological features. We develop the distance transform for three-class pathology and two-class radiology images to reveal various tumor patterns. We use persistent homology to quantify shape information and provide potential clinical interpretation of computed topological features. The topological persistence information is represented as functional data and used to fit the FCoxPH model to predict the survival prognosis of lung adenocarcinoma and GBM patients. The topological features are shown to have a significant non-zero effect on the hazard function. Also, the topological signals included in the FCoxPH model improve the predictive accuracy over the CoxPH model. This suggests that the proposed topological features well summarize tumor aggressiveness.

Our study leads to several interesting topics for future research. First, while we found

a relationship between the topological shape features and survival prognosis, a complex relationship between the shape features, clinical variables, and genetic features are largely unknown. Recent studies investigate the relationships between imaging features and gene expressions; using the radiomic features of pancreatic ductal adenocarcinoma (Li et al., 2019) and the degree of tumor eccentricity of breast cancer (Moon et al., 2015). The future research topic will include exploring the association of topological shape features with gene expressions. Second, one of the drawbacks of the proposed persistent homology approach is that it loses tumor location information. This is suitable for the lung adenocarcinoma application that the images do not have a pre-determined direction. However, the tumor spatial information could be important in some cancer image analyses, such as brain tumor (Bondy et al., 2008). In the future, it would be useful to pair spatial information with the topological features computed by persistent homology. Lastly, our method can easily be applied to 3D medical images. In the 3D applications, three-dimensional persistent homology summaries of zero-, one-, and two-dimensional topological features will be obtained, and the size of 3D topological shape features will be measured by the radius of the largest sphere.

Data Availability

Three examples of NLST lung cancer pathology images of Wang et al. (2018) are available from the repository <https://github.com/chulmoon/TopologicalTumorShape> and the binary GBM MRI images are available from the repository <https://github.com/loriananthony/SECT>.

Software Availability

Software is publicly available in Python (persistent homology computation) and R (functional representation and modeling) code, and located on the repository <https://github.com/chulmoon/TopologicalTumorShape>.

Declaration of Interests

The authors declare that they have no conflict of interest.

References

Adams, H., Emerson, T., Kirby, M., Neville, R., Peterson, C., Shipman, P., Chepushtanova, S., Hanson, E., Motta, F., and Ziegelmeier, L. (2017), “Persistence images: a stable vector representation of persistent homology,” *Journal of Machine Learning Research*, 18, 1–35.

Adcock, A., Carlsson, E., and Carlsson, G. (2016), “The ring of algebraic functions on persistence bar codes,” *Homology, Homotopy and Applications*, 18, 381–402.

Bendich, P., Chin, S. P., Clark, J., Desena, J., Harer, J., Munch, E., Newman, A., Porter, D., Rouse, D., Strawn, N., and Watkins, A. (2016), “Topological and statistical behavior classifiers for tracking applications,” *IEEE Transactions on Aerospace and Electronic Systems*, 52, 2644–2661.

Berry, E., Chen, Y.-C., Cisewski-Kehe, J., and Fasy, B. T. (2020), “Functional summaries of persistence diagrams,” *Journal of Applied and Computational Topology*, 4, 211–262.

Bharath, K., Kurtek, S., Rao, A., and Baladandayuthapani, V. (2018), “Radiologic image-based statistical shape analysis of brain tumours,” *Journal of the Royal Statistical Society: Series C (Applied Statistics)*, 67, 1357–1378.

Bianconi, F., Fravolini, M. L., Bello-Cerezo, R., Minestrini, M., Scialpi, M., and Palumbo, B. (2018), “Evaluation of shape and textural features from CT as prognostic biomarkers in non-small cell lung cancer,” *Anticancer Research*, 38, 2155–2160.

Bondy, M. L., Scheurer, M. E., Malmer, B., Barnholtz-Sloan, J. S., Davis, F. G., Il’Yasova, D., Kruchko, C., McCarthy, B. J., Rajaraman, P., Schwartzbaum, J. A., et al. (2008), “Brain tumor epidemiology: consensus from the Brain Tumor Epidemiology Consortium,” *Cancer*, 113, 1953–1968.

Bookstein, F. L. (1997), *Morphometric tools for landmark data: geometry and biology*, Cambridge University Press.

Brú, A., Casero, D., De Franciscis, S., and Herrero, M. A. (2008), “Fractal analysis and tumour growth,” *Mathematical and Computer Modelling*, 47, 546–559.

Bubenik, P. (2015), “Statistical topological data analysis using persistence landscapes,” *Journal of Machine Learning Research*, 16, 77–102.

Carlsson, G. (2009), “Topology and data,” *Bulletin of the American Mathematical Society*, 46, 255–308.

Chatzistamou, I., Rodriguez, J., Jouffroy, T., Girod, A., Point, D., Sklavounou, A., Kittas, C., Sastre-Garau, X., and Klijanienko, J. (2010), “Prognostic significance of tumor shape and stromal chronic inflammatory infiltration in squamous cell carcinomas of the oral tongue,” *Journal of Oral Pathology & Medicine*, 39, 667–671.

Chazal, F., Fasy, B., Lecci, F., Michel, B., Rinaldo, A., Rinaldo, A., and Wasserman, L. (2017), “Robust topological inference: distance to a measure and kernel distance,” *Journal of Machine Learning Research*, 18, 5845–5884.

Chazal, F., Fasy, B. T., Lecci, F., Rinaldo, A., and Wasserman, L. (2014), “Stochastic convergence of persistence landscapes and silhouettes,” in *Proceedings of the thirtieth annual symposium on Computational geometry*, pp. 474–483.

Chen, A. X. and Rabadán, R. (2017), “A fast semi-automatic segmentation tool for processing brain tumor images,” in *Towards Integrative Machine Learning and Knowledge Extraction*, Springer, pp. 170–181.

Chen, K., Chen, K., Müller, H.-G., and Wang, J.-L. (2011), “Stringing high-dimensional data for functional analysis,” *Journal of the American Statistical Association*, 106, 275–284.

Chen, Y.-C., Wang, D., Rinaldo, A., and Wasserman, L. (2015), “Statistical analysis of persistence intensity functions,” *arXiv e-prints*.

Clark, K., Vendt, B., Smith, K., Freymann, J., Kirby, J., Koppel, P., Moore, S., Phillips, S., Maffitt, D., Pringle, M., et al. (2013), “The Cancer Imaging Archive (TCIA): maintaining and operating a public information repository,” *Journal of Digital Imaging*, 26, 1045–1057.

Couprise, M., Bezerra, F.-N., and Bertrand, G. (2001), “Topological operators for grayscale image processing,” *Journal of Electronic Imaging*, 10, 1003 – 1015.

Cox, D. R. (1972), “Regression models and life-tables,” *Journal of the Royal Statistical Society. Series B (Methodological)*, 34, 187–220.

Crawford, L., Monod, A., Chen, A. X., Mukherjee, S., and Rabadán, R. (2020), “Predicting clinical outcomes in glioblastoma: an application of topological and functional data analysis,” *Journal of the American Statistical Association*, 115, 1139–1150.

Dlotko, P. (2015), “Cubical complex,” in *GUDHI User and Reference Manual*, GUDHI Editorial Board.

Edelsbrunner, H. and Harer, J. (2008), “Persistent homology - a survey,” *Contemporary Mathematics*, 453, 257–282, Surveys on Discrete and Computational Geometry: Twenty Years Later. Providence, IMS.

Efron, B. (1977), “The efficiency of Cox’s likelihood function for censored data,” *Journal of the American Statistical Association*, 72, 557–565.

Eisenhauer, E. A., Therasse, P., Bogaerts, J., Schwartz, L. H., Sargent, D., Ford, R., Dancey, J., Arbuck, S., Gwyther, S., Mooney, M., et al. (2009), “New response evaluation criteria in solid tumours: revised RECIST guideline (version 1.1),” *European Journal of Cancer*, 45, 228–247.

Gellar, J. E., Colantuoni, E., Needham, D. M., and Crainiceanu, C. M. (2015), “Cox regression models with functional covariates for survival data,” *Statistical Modelling*, 15, 256–278.

Gillies, R. J., Kinahan, P. E., and Hricak, H. (2016), “Radiomics: images are more than pictures, they are data,” *Radiology*, 278, 563–577.

Grove, O., Berglund, A. E., Schabath, M. B., Aerts, H. J., Dekker, A., Wang, H., Velazquez, E. R., Lambin, P., Gu, Y., Balagurunathan, Y., et al. (2015), “Quantitative computed tomographic descriptors associate tumor shape complexity and intratumor heterogeneity with prognosis in lung adenocarcinoma,” *PloS one*, 10, e0118261.

Hammoud, M. A., Sawaya, R., Shi, W., Thall, P. F., and Leeds, N. E. (1996), “Prognostic significance of preoperative MRI scans in glioblastoma multiforme,” *Journal of neuro-oncology*, 27, 65–73.

Hao, M., Liu, K.-y., Xu, W., and Zhao, X. (2020), “Semiparametric inference for the functional Cox model,” *Journal of the American Statistical Association*, 1–11.

Happ, C. and Greven, S. (2018), “Multivariate functional principal component analysis for data observed on different (dimensional) domains,” *Journal of the American Statistical Association*, 113, 649–659.

Haralick, R. M., Shanmugam, K., and Dinstein, I. (1973), “Textural features for image classification,” *IEEE Transactions on Systems, Man, and Cybernetics*, SMC-3, 610–621.

Havaei, M., Davy, A., Warde-Farley, D., Biard, A., Courville, A., Bengio, Y., Pal, C., Jodoin, P.-M., and Larochelle, H. (2017), “Brain tumor segmentation with deep neural networks,” *Medical Image Analysis*, 35, 18–31.

Henson, J. W., Gaviani, P., and Gonzalez, R. G. (2005), “MRI in treatment of adult gliomas,” *The lancet oncology*, 6, 167–175.

Hörmann, S., Kidziński, L., and Hallin, M. (2015), “Dynamic functional principal components,” *Journal of the Royal Statistical Society: Series B (Statistical Methodology)*, 77, 319–348.

Karhunen, K. (1947), “Über lineare Methoden in der Wahrscheinlichkeitsrechnung,” *Annales Academiae Scientiarum Fennicae Series A*, 37, 1–79.

Kilday, J., Palmieri, F., and Fox, M. D. (1993), “Classifying mammographic lesions using computerized image analysis,” *IEEE transactions on medical imaging*, 12, 664–669.

Kong, D., Ibrahim, J. G., Lee, E., and Zhu, H. (2018), “FLCRM: Functional linear cox regression model,” *Biometrics*, 74, 109–117.

Kusano, G., Hiraoka, Y., and Fukumizu, K. (2016), “Persistence weighted Gaussian kernel for topological data analysis,” *Proceedings of The 33rd International Conference on Machine Learning*, 48, 2004–2013.

Lawson, P., Sholl, A., Brown, J., Fasy, B. T., and Wenk, C. (2019), “Persistent Homology for the Quantitative Evaluation of Architectural Features in Prostate Cancer Histology,” *Scientific Reports*, 9, 1139.

Lee, E., Zhu, H., Kong, D., Wang, Y., Sullivan Giovanello, K., Ibrahim, J. G., and Neuroimaging Initiative, f. t. A. D. (2015), “BFLCRM: A Bayesian functional linear Cox regression model for predicting time to conversion to Alzheimer’s disease,” *Annals of Applied Statistics*, 9, 2153–2178.

Levine, A. B., Schlosser, C., Grewal, J., Coope, R., Jones, S. J., and Yip, S. (2019), “Rise of the machines: advances in deep learning for cancer diagnosis,” *Trends in Cancer*, 5, 157–169.

Li, K., Xiao, J., Yang, J., Li, M., Xiong, X., Nian, Y., Qiao, L., Wang, H., Eresen, A., Zhang, Z., et al. (2019), “Association of radiomic imaging features and gene expression profile as prognostic factors in pancreatic ductal adenocarcinoma,” *American Journal of Translational Research*, 11, 4491.

Loève, M. (1946), “Fonctions aléatoires à décomposition orthogonale exponentielle,” *La Revue Scientifique*, 84, 159–162.

Madabhushi, A. and Lee, G. (2016), “Image analysis and machine learning in digital pathology: Challenges and opportunities,” *Medical Image Analysis*, 33, 170–175.

Matsuda, T. and Machii, R. (2015), “Morphological distribution of lung cancer from Cancer Incidence in Five Continents Vol. X,” *Japanese Journal of Clinical Oncology*, 45, 404–404.

Miller, T. R., Pinkus, E., Dehdashti, F., and Grigsby, P. W. (2003), “Improved prognostic value of 18F-FDG PET using a simple visual analysis of tumor characteristics in patients with cervical cancer,” *Journal of Nuclear Medicine*, 44, 192–197.

Moon, C., Mitchell, S. A., Heath, J. E., and Andrew, M. (2019), “Statistical inference over persistent homology predicts fluid flow in porous media,” *Water Resources Research*, 55, 9592–9603.

Moon, H.-G., Kim, N., Jeong, S., Lee, M., Moon, H., Kim, J., Yoo, T.-K., Lee, H.-B., Kim, J., Noh, D.-Y., et al. (2015), “The clinical significance and molecular features of the spatial tumor shapes in breast cancers,” *PLoS one*, 10, e0143811.

Müller, H.-G. and Stadtmüller, U. (2005), “Generalized functional linear models,” *Annals of Statistics*, 33, 774–805.

Nelson, J., Tsukada, Y., Schoenfeld, D., Fulling, K., Lamarche, J., and Peress, N. (1983), “Necrosis as a prognostic criterion in malignant supratentorial, astrocytic gliomas,” *Cancer*, 52, 550–554.

Network, C. G. A. R. et al. (2008), “Comprehensive genomic characterization defines human glioblastoma genes and core pathways,” *Nature*, 455, 1061.

Oyama, A., Hiraoka, Y., Obayashi, I., Saikawa, Y., Furui, S., Shiraishi, K., Kumagai, S., Hayashi, T., and Kotoku, J. (2019), “Hepatic tumor classification using texture and topology analysis of non-contrast-enhanced three-dimensional T1-weighted MR images with a radiomics approach,” *Scientific Reports*, 9, 1–10.

Qaiser, T., Sirinukunwattana, K., Nakane, K., Tsang, Y.-W., Epstein, D., and Rajpoot, N. (2016), “Persistent Homology for Fast Tumor Segmentation in Whole Slide Histology Images,” *Procedia Computer Science*, 90, 119 – 124.

Qu, S., Wang, J.-L., and Wang, X. (2016), “Optimal estimation for the functional Cox model,” *Ann. Statist.*, 44, 1708–1738.

Raza, S. M., Lang, F. F., Aggarwal, B. B., Fuller, G. N., Wildrick, D. M., and Sawaya, R. (2002), “Necrosis and glioblastoma: a friend or a foe? A review and a hypothesis,” *Neurosurgery*, 51, 2–13.

Reininghaus, J., Huber, S. M., Bauer, U., and Kwitt, R. (2015), “A stable multi-scale kernel for topological machine learning,” *2015 IEEE Conference on Computer Vision and Pattern Recognition*, 4741–4748.

Rizzo, S., Botta, F., Raimondi, S., Origgi, D., Fanciullo, C., Morganti, A. G., and Belomi, M. (2018), “Radiomics: the facts and the challenges of image analysis,” *European radiology experimental*, 2, 1–8.

Robins, V., Saadatfar, M., Delgado-Friedrichs, O., and Sheppard, A. P. (2016), “Percolating length scales from topological persistence analysis of micro-CT images of porous materials,” *Water Resources Research*, 52, 315–329.

Scarpase, L., Mikkelsen, L., Cha, T., Rao, S., Tekchandani, S., Gutman, S., and Pierce, D. (2016), “Radiology data from the cancer genome atlas glioblastoma multiforme [TCGA-GBM] collection,” *The Cancer Imaging Archive*, 11, 1.

Sefidgar, M., Soltani, M., Raahemifar, K., Bazmara, H., Nayinian, S. M. M., and Bazargan, M. (2014), “Effect of tumor shape, size, and tissue transport properties on drug delivery to solid tumors,” *Journal of Biological Engineering*, 8, 12.

Siegel, R. L., Miller, K. D., and Jemal, A. (2020), “Cancer statistics, 2020,” *CA: A Cancer Journal for Clinicians*, 70, 7–30.

Soltani, M. and Chen, P. (2012), “Effect of tumor shape and size on drug delivery to solid tumors,” *Journal of Biological Engineering*, 6, 4.

Somasundaram, E., Litzler, A., Wadhwa, R., and Scott, J. (2021), “BIO21-010: Lung cancer survival is associated with persistent homology of tumor imaging,” *Journal of the National Comprehensive Cancer Network*, 19, BIO21–010.

Surawicz, T. S., McCarthy, B. J., Kupelian, V., Jukich, P. J., Bruner, J. M., and Davis, F. G. (1999), “Descriptive epidemiology of primary brain and CNS tumors: results from

the Central Brain Tumor Registry of the United States, 1990-1994,” *Neuro-oncology*, 1, 14–25.

Upadhyay, N. and Waldman, A. (2011), “Conventional MRI evaluation of gliomas,” *The British Journal of Radiology*, 84, S107–S111.

Vogl, T. J., Worst, T. S., Naguib, N. N., Ackermann, H., Gruber-Rouh, T., and Nour-Eldin, N.-E. A. (2013), “Factors influencing local tumor control in patients with neoplastic pulmonary nodules treated with microwave ablation: a risk-factor analysis,” *American Journal of Roentgenology*, 200, 665–672.

Wang, S., Chen, A., Yang, L., Cai, L., Xie, Y., Fujimoto, J., Gazdar, A., and Xiao, G. (2018), “Comprehensive analysis of lung cancer pathology images to discover tumor shape and boundary features that predict survival outcome,” *Scientific Reports*, 8, 10393.

Wang, S., Yang, D. M., Rong, R., Zhan, X., and Xiao, G. (2019), “Pathology image analysis using segmentation deep learning algorithms,” *The American journal of pathology*, 189, 1686–1698.

Yao, F., Müller, H.-G., and Wang, J.-L. (2005), “Functional data analysis for sparse longitudinal data,” *Journal of the American Statistical Association*, 100, 577–590.

Yokoyama, I., Sheahan, D., Carr, B., Kakizoe, S., Selby, R., Tzakis, A., Todo, S., Iwatsuki, S., and Starzl, T. (1991), “Clinicopathologic factors affecting patient survival and tumor recurrence after orthotopic liver transplantation for hepatocellular carcinoma,” *Transplantation Proceedings*, 23, 2194–2196.

Zappa, C. and Mousa, S. A. (2016), “Non-small cell lung cancer: current treatment and future advances,” *Translational Lung Cancer Research*, 5, 288.

Zhang, C., Xiao, G., Moon, C., Chen, M., and Li, Q. (2020), “Bayesian landmark-based shape analysis of tumor pathology images,” *arXiv preprint arXiv:2012.01149*.

Zhu, X., Li, K., Kamaly-Asl, I., Checkley, D., Tessier, J., Waterton, J., and Jackson, A. (2000), “Quantification of endothelial permeability, leakage space, and blood volume

in brain tumors using combined T1 and T2* contrast-enhanced dynamic MR imaging," *Journal of Magnetic Resonance Imaging: An Official Journal of the International Society for Magnetic Resonance in Medicine*, 11, 575–585.

Supplementary Material

Persistent Homology for Multi-class Medical Images

Persistent Homology Computation

We illustrate the proposed persistent homology approach for medical images with the three-class tumor image example. First, Figure S1a presents the three-class example image where the green-, blue-, and yellow-colored pixels are tumor, normal, and empty regions, respectively. Figure S1b shows the signed distance transformed values assigned for each pixel. Here, a taxicab metric is used instead of a Euclidean distance for convenience.

We construct cubical complices using the signed distance. Let \mathcal{C}_ϵ be the cubical complex with filtration ϵ . In \mathcal{C}_ϵ , the pixels whose assigned distances are less than ϵ enter the complex. Figures from S1c to S1h in Supplementary Material present the sequence of cubical complices with $\epsilon \in \{-3, -2, \dots, 3\}$.

In Figure S1 example, two dimension-zero features (i.e., connected components) are recorded. The first dimension-zero feature appears in \mathcal{C}_{-3} in the bottom-left corner of Figure S1c and the second dimension-zero feature is created in \mathcal{C}_{-1} in the middle of Figure S1e. Two components are connected in \mathcal{C}_1 so the second feature dies at $\epsilon = 1$. Also, we observe three dimension-one features (i.e., loops) in the example. Two holes show up in \mathcal{C}_{-1} in the middle of Figure S1e. The smaller hole disappears in \mathcal{C}_1 and the larger hole is filled in \mathcal{C}_2 . The other dimension-one component appears in \mathcal{C}_1 and disappears in \mathcal{C}_2 .

The birth and death information of topological features explained above is summarized in persistent diagrams in Figures S1i and S1j.

Interpretation of Persistent Homology Computation Result

Persistent homology computation results summarize various tumor shape patterns. Dimension-zero features appear in the three non-zero quadrants of persistence diagrams: 1) quadrant II (e.g., A, B, C, and D of Figure 4 in the main article); 2) quadrant I (e.g., E and F of Figure 4 in the main article); and 3) and quadrant III (e.g., G, H, and I of Figure 4 in the

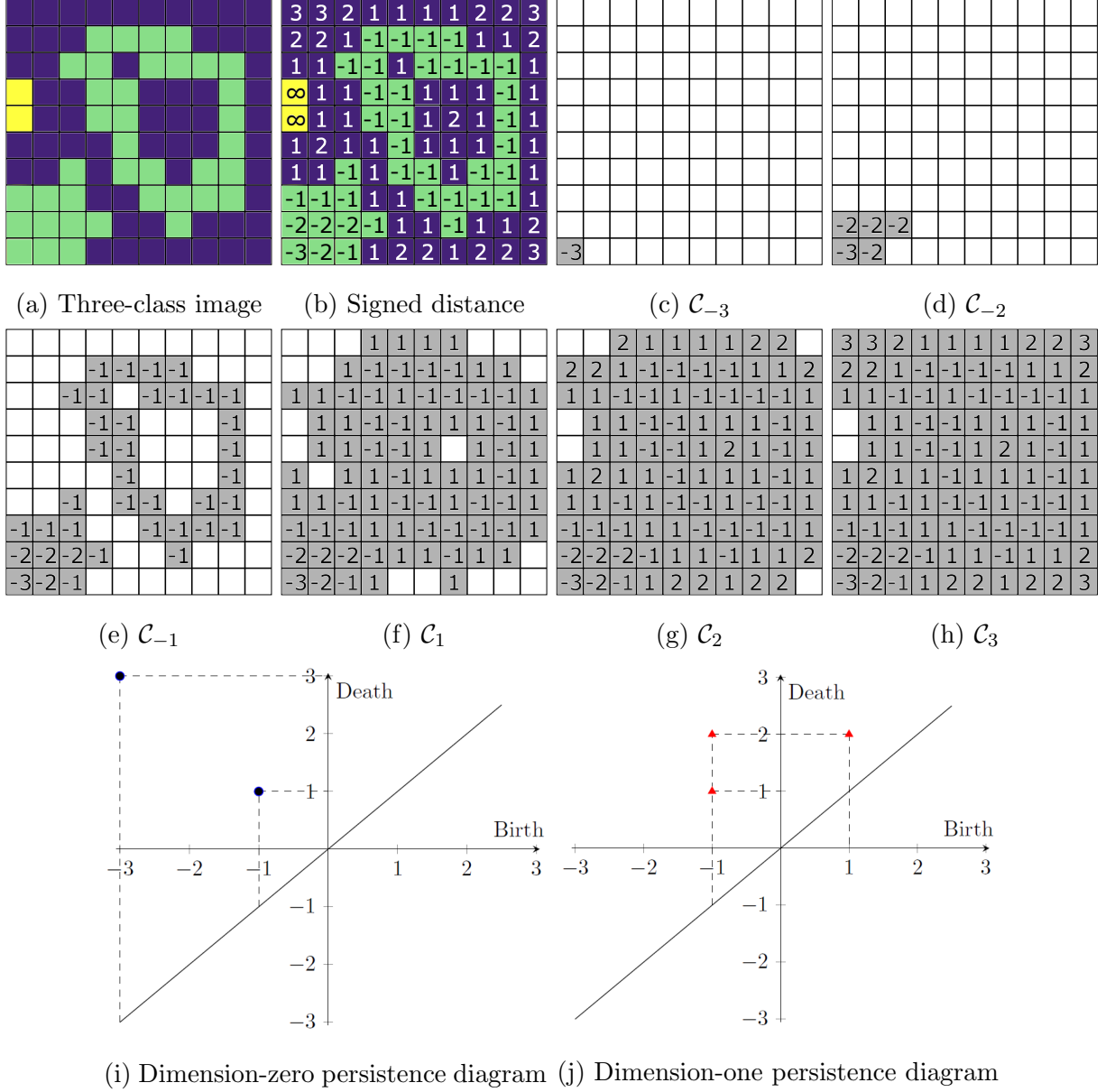


Figure S1: (a): Three-class example image. The green-, blue-, and yellow-colored pixels are tumor, normal, and empty regions, respectively. (b): Signed distances using the taxicab distance. (c)-(h): a sequence of cubical complices based on the computed signed distance. The pixels included in the cubical complices are marked in gray. (i)-(j): dimension zero- and one-persistence diagrams.

main article). First, the scattered tumors are recorded in quadrant II. The larger the tumor regions, the larger birth values are in quadrant II (e.g., A vs. B and C vs. D of Figure 4 in

the main article). Also, larger death values imply that distances between the disconnected tumor regions are far from each other (e.g., A vs. C and B vs. D of Figure 4 in the main article). Second, quadrant I represents the separate normal regions that include tumor regions. Death values are proportional to the distance between the boundary of normal regions and the tumor regions inside (e.g., E vs. F of Figure 4 in the main article). Third, connected tumor regions appear in quadrant III. The birth values are the size of tumor regions (e.g., G vs. H of Figure 4 in the main article), and the death values are the size of the contact area of two tumor regions (e.g., G vs. I of Figure 4 in the main article). The death value illustrates how close the tumor regions are. The connected tumor regions can be in different shapes. For example, they could be a series of overlapped tumor regions (left figures of G, H, and I of Figure 4 in the main article) or tumor regions that have normal regions inside (right figures of G, H, and I of Figure 4 in the main article).

Dimension-one features are summarized in two quadrants: 1) quadrant II (e.g., J, K, L, and M of Figure 4 in the main article); and 2) quadrant I (e.g., N, O, and P of Figure 4 in the main article). First, the normal regions surrounded by the tumor regions appear in quadrant II. Here, the large negative birth value means the surrounding tumor regions are thick (e.g., J vs. K and L vs. M of Figure 4 in the main article), and the large death value means the trapped normal regions are large (e.g., J vs. L and K vs. M of Figure 4 in the main article). Second, the broken-ring-shaped or double-broken-ring-shaped tumor regions are recorded in quadrant I. The large birth values imply that there are large gaps in the broken-ring or double-broken-ring-shaped shaped regions (e.g., N vs. O of Figure 4 in the main article). Also, the large death value means the size of the inside of the broken-ring or double-broken-ring shape is large (e.g., N vs. P of Figure 4 in the main article).

Case Studies Results

Smoothing Parameters for Persistence Surface Functions

Tables S1 and S2 list smoothing parameters selected by the Leave-One-Out Cross-Validation (LOOCV).

Table S1: Smoothing parameters of dimension-zero (σ_0) and dimension-one (σ_1) persistence surface functions selected by the LOOCV for the lung cancer pathology image case study. The smoothing parameters used in the case study are in bold.

σ_0	σ_1
1.3	1
1.4	0.9, 1
1.5	0.8, 0.9, 1
1.6	0.8, 0.9, 1
1.7	0.8, 0.9, 1, 1.1
1.8	0.8, 0.9, 1, 1.1
1.9	0.8, 0.9, 1, 1.1
2.0	0.8, 0.9 , 1, 1.1
2.1	0.8, 0.9, 1.1
2.2	0.8, 0.9, 1, 1.1
2.3	0.8, 0.9, 1, 1.1
2.4	0.8, 0.9, 1
2.5	0.8

Table S2: Smoothing parameters of dimension-zero (σ_0) and dimension-one (σ_1) persistence surface functions selected by the LOOCV for the GBM MRI image case study. The smoothing parameters used in the case study are in bold.

σ_0	σ_1
0.1	0.1, 0.2, 0.3, 0.5, 0.6, 0.7, 0.8, 0.9
0.2	0.1, 0.2, 0.3, 0.5, 0.6, 0.7, 0.8, 0.9
0.3	0.1, 0.2, 0.3, 0.5 , 0.6, 0.7, 0.8, 0.9
0.4	0.5, 0.6, 0.7, 0.8, 0.9
0.5	0.6, 0.7, 0.8, 0.9

P-values of the FCoxPH models with False Shape Images

Figures S2 and S3 present the distribution of p-values of the log-rank tests of the FCoxPH models using the rearranged images for lung pathology images and brain MRI images, re-

spectively. The p-value of the CoxPH model is given as a dotted line. Most p-values of the FCoxPH models remain similar to the p-value of the CoxPH model even though the false shape information is used.

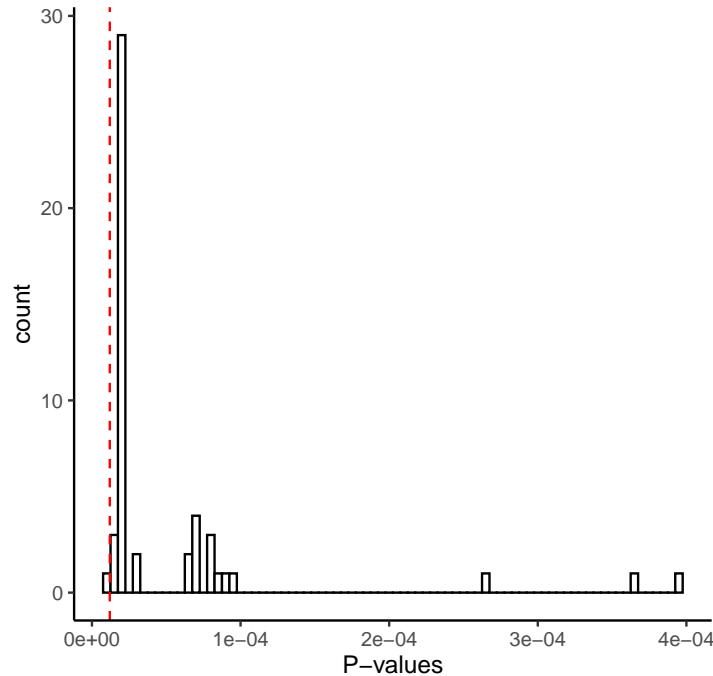


Figure S2: The p-values of the FCoxPH models with pixel-rearranged lung pathology images. The dotted line is drawn at the p-value of the CoxPH model.

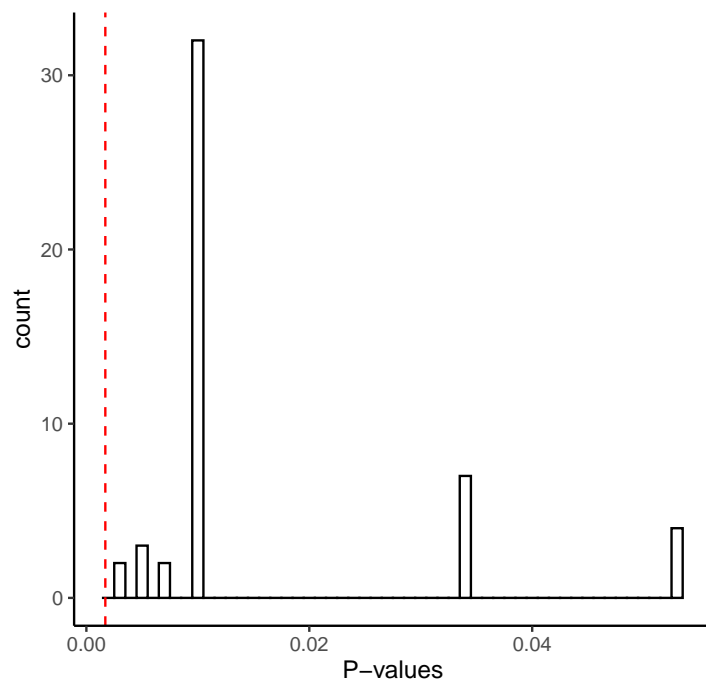


Figure S3: The p-values of the FCoxPH models with pixel-rearranged brain MRI images. The dotted line is drawn at the p-value of the CoxPH model.